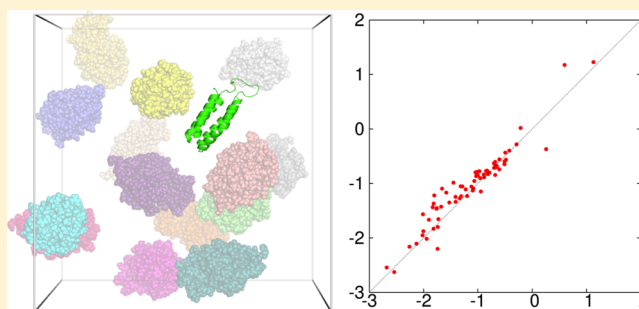


# Further Development of the FFT-based Method for Atomistic Modeling of Protein Folding and Binding under Crowding: Optimization of Accuracy and Speed

Sanbo Qin and Huan-Xiang Zhou\*

Department of Physics and Institute of Molecular Biophysics, Florida State University, Tallahassee, Florida, United States

**ABSTRACT:** Recently, we (Qin, S.; Zhou, H. X. *J. Chem. Theory Comput.* **2013**, 9, 4633–4643) developed the FFT-based method for Modeling Atomistic Proteins–crowder interactions, henceforth FMAP. Given its potential wide use for calculating effects of crowding on protein folding and binding free energies, here we aimed to optimize the accuracy and speed of FMAP. FMAP is based on expressing protein–crowder interactions as correlation functions and evaluating the latter via fast Fourier transform (FFT). The numerical accuracy of FFT improves as the grid spacing for discretizing space is reduced, but at increasing computational cost. We sought to speed up FMAP calculations by using a relatively coarse grid spacing of 0.6 Å and then correcting for discretization errors. This strategy was tested for different types of interactions (hard-core repulsion, nonpolar attraction, and electrostatic interaction) and over a wide range of protein–crowder systems. We were able to correct for the numerical errors on hard-core repulsion and nonpolar attraction by an 8% inflation of atomic hard-core radii and on electrostatic interaction by a 5% inflation of the magnitudes of protein atomic charges. The corrected results have higher accuracy and enjoy a speedup of more than 100-fold over those obtained using a fine grid spacing of 0.15 Å. With this optimization of accuracy and speed, FMAP may become a practical tool for realistic modeling of protein folding and binding in cell-like environments.



## 1. INTRODUCTION

In cellular compartments, the presence of high concentrations of bystander macromolecules (or crowders) may significantly affect protein folding and binding free energies.<sup>1–3</sup> Earlier modeling of crowding effects focused on hard-core repulsion between the test protein and the crowders.<sup>1,4–13</sup> Recent experimental studies have shown that soft interactions, operating at longer range and having weaker distance dependence, can counterbalance the effect of hard-core repulsion.<sup>14–22</sup> The balancing act of hard-core and soft interactions has been reinforced by computational studies and theoretical analyses.<sup>23–28</sup>

That the net effects of crowding are determined by the balance of hard-core and soft interactions increases the complexity of modeling such effects and raises the level of accuracy necessary when one aims to model protein–crowder systems of experimental studies. In the past, many computational studies have treated the test protein at a coarse-grained level and the crowders as spherical particles.<sup>4,5,10–12,26</sup> An approach in which protein conformations from crowder-free simulations are weighted by the excess chemical potential of the protein has opened the door for modeling effects of crowding at the atomic level.<sup>6,7,22,25</sup> This “postprocessing” approach<sup>7</sup> predicts the change in the folding or binding free energy by crowding, not the latter quantity itself. The excess chemical

potential,  $\Delta\mu(\mathbf{X})$ , arises from interactions with crowders and is given by<sup>29,30</sup>

$$\exp(-\Delta\mu(\mathbf{X})/k_B T) = \langle \exp[-U_{\text{int}}(\mathbf{X}, \mathbf{R})/k_B T] \rangle_{\mathbf{R},c} \quad (1)$$

where  $U_{\text{int}}(\mathbf{X}, \mathbf{R})$  is the protein–crowder interaction energy for protein conformation  $\mathbf{X}$  and position  $\mathbf{R}$  inside the crowder solution,  $k_B$  is Boltzmann’s constant,  $T$  is the absolute temperature, and  $\langle \dots \rangle_{\mathbf{R},c}$  means averaging over the position of the test protein and the configuration of the crowders. Implementation of this approach by brute-force calculations of  $\Delta\mu(\mathbf{X})$  turned out to be extremely expensive.<sup>25</sup> Recently we developed a method that allows the full potential of the postprocessing approach to be realized.<sup>31</sup> This method is based on expressing the protein–crowder interactions as correlation functions and evaluating the latter via fast Fourier transform (FFT).

In this FMAP (FFT-based Modeling of Atomistic Proteins–crowder interactions) method, both the protein position and the protein–crowder interaction functions are discretized on a grid. Both types of discretization errors can be reduced by

**Special Issue:** Free Energy Calculations: Three Decades of Adventure in Chemistry and Biophysics

**Received:** March 4, 2014

**Published:** May 6, 2014

decreasing the grid spacing, but at increased computational cost. The aim of the present study was to optimize the accuracy and speed of FMAP. Our tests through exhaustively enumerating all protein–crowder atom pairs, referred to as the atom-based method (similar to the brute-force method of McGuffee and Elcock<sup>25</sup>), which is free of the errors from mapping the interaction functions to the grid, showed that the errors from discretizing protein positions become negligible at a 0.6 Å grid spacing. On the other hand, errors from discretizing the interaction functions in FMAP calculations persist even to a 0.15 Å grid spacing, although extrapolation to 0 grid spacing reaches agreement with the atom-based method. However, we were able to correct for the latter type of discretization errors. The corrected results have higher accuracy and enjoy a speedup of more than 100-fold over those obtained using a fine grid spacing of 0.15 Å. This optimization of accuracy and speed positions FMAP for wide usage for realistic modeling of protein folding and binding in cell-like environments and may be instructive for improving other methods that employ discretization of space.

## 2. COMPUTATIONAL DETAILS

**2.1. The Interaction Energy.** The protein–crowder interaction energy is a potential of mean force, with other solvent degrees of freedom averaged out. Our potential function consisted of the Lennard-Jones and Debye–Hückel potentials, which are commonly used to model intermolecular interactions.<sup>25,32–35</sup> Specifically, we modeled steric, van der Waals, and hydrophobic interactions together using the Lennard-Jones potential

$$U_{\text{LJ}} = \sum_{ij} (A_{ij}/r_{ij}^{12} - B_{ij}/r_{ij}^6) \\ = \sum_{ij} 4\epsilon_{ij}[(\sigma_{ij}/r_{ij})^{12} - (\sigma_{ij}/r_{ij})^6] \quad (2)$$

where  $r_{ij}$  denotes the distance between crowder atom  $i$  and protein atom  $j$ . We refer to  $\sigma_{ii}/2$  as the hard-core radius of atom  $i$  and  $d_{ij} \equiv (\sigma_{ii} + \sigma_{jj})/2$  as the distance of closest approach between atoms  $i$  and  $j$ . Electrostatic interactions were modeled by the Debye–Hückel potential

$$U_{\text{DH}} = \sum_{ij} q_i q_j \exp(-r_{ij}/\lambda) / \kappa r_{ij} \quad (3)$$

where  $q_i$  are atomic charges and  $\lambda$  and  $\kappa$  are the Debye screening length and the dielectric constant, respectively, of the crowder solution.

In calculating  $\Delta\mu(X)$ , the test protein could be placed anywhere in the crowder solution, including positions where  $r_{ij}$  approaches zero, and hence  $U_{\text{LJ}}$  (as well as  $U_{\text{DH}}$ ) has exceedingly large magnitudes. Partly to minimize possible numerical uncertainties associated with such positions, we split  $U_{\text{LJ}}$  into a steric term  $U_{\text{st}}$  and a nonpolar attraction term  $U_{\text{na}}$  (Figure 1):

$$U_{\text{st}} = \infty \text{ if any } r_{ij} < d_{ij} \\ = 0 \text{ if all } r_{ij} > d_{ij} \quad (4)$$

and

$$U_{\text{na}} = 0 \text{ if any } r_{ij} < d_{ij} \\ = U_{\text{LJ}} \text{ if all } r_{ij} > d_{ij} \quad (5)$$

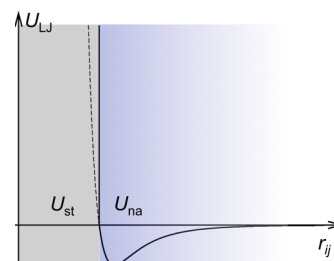


**Figure 1.** Split of  $U_{\text{LJ}}$  into  $U_{\text{st}}$  and  $U_{\text{na}}$  at  $r_{ij} = d_{ij}$ , when only a pair of atoms is considered. If the two atoms are of the same type, then  $d_{ij} = \sigma_{ij}$ ; the latter is the interatomic distance where  $U_{\text{LJ}} = 0$ . For two different types of atoms,  $d_{ij}$  is slightly larger than  $\sigma_{ij}$ , and hence when the split is triggered,  $U_{\text{na}}$  would be slightly negative instead of 0.

When  $d_{ij} = \sigma_{ij}$  (true, e.g., for the interaction between two atoms of the same type), the split of  $U_{\text{LJ}}$  into  $U_{\text{st}}$  and  $U_{\text{na}}$  occurs where  $U_{\text{LJ}} = 0$ . We also set  $U_{\text{DH}}$  to 0 if any  $r_{ij} < d_{ij}$ , thus stipulating that the Debye–Hückel potential operated only when the protein was free of steric clash with the crowders. The resulting total interaction energy is

$$U_{\text{int}} = U_{\text{st}} + U_{\text{na}} + U_{\text{DH}} \quad (6)$$

$U_{\text{st}}$  represents the hard-core repulsion, while  $U_{\text{na}}$  and  $U_{\text{DH}}$  are soft interactions.

We emphasize that the steric term is triggered not at the level of each protein–crowder atom pair but globally, i.e., when all the atom pairs are considered. If at least one atom pair has  $r_{ij} < d_{ij}$ , then the protein is labeled as clashing with the crowders, and the steric term is imposed and the soft interactions are turned off. In practice, we first evaluated the soft interactions without considering clash. Based on a separate detection for clash, we then decided on using either the steric term or the soft interactions for the total interaction energy. To avoid floating-point overflow, we set the values of the soft interactions for atom pairs at  $r_{ij} < 1$  Å to the values at  $r_{ij} = 1$  Å. This treatment did not introduce any errors since the soft interactions at  $r_{ij} < 1$  Å would not be used ultimately, as any  $r_{ij} < 1$  Å would trigger the clash condition.

We used Autodock parameters<sup>34</sup> for the Lennard-Jones potential ( $\epsilon_{\alpha\alpha}$  and  $\sigma_{\alpha\alpha}$  of atom type  $\alpha$ ) and Amber parameters<sup>36</sup> for the atomic charges ( $q_\alpha$ ). For Lennard-Jones interactions between different atom types, we used the combination rule  $\epsilon_{\alpha\beta} = (\epsilon_{\alpha\alpha}\epsilon_{\beta\beta})^{1/2}$  and  $\sigma_{\alpha\beta} = (\sigma_{\alpha\alpha}\sigma_{\beta\beta})^{1/2}$ . This combination allows the two terms of the Lennard-Jones potential to be written as correlation functions (see below) and hence evaluation via FFT. The resulting  $\sigma_{\alpha\beta}$  is slightly less than the distance of closet approach  $d_{\alpha\beta}$  defined above; so for the interaction between two different types of atoms, the split of  $U_{\text{LJ}}$  into  $U_{\text{st}}$  and  $U_{\text{na}}$  occurs at an interatomic distance where  $U_{\text{LJ}}$  is slightly negative. We used the dielectric constant of pure water for  $\kappa$ , but to achieve a better balance between  $U_{\text{na}}$  and  $U_{\text{DH}}$ , we scaled  $U_{\text{na}}$  down 5-fold and scaled  $U_{\text{DH}}$  up 2-fold. Parameter tuning to achieve agreement with experimental measurements is left for future studies.

**2.2. Discretizing the Protein Position on a Grid and the Atom-based Method.** The averaging in eq 1 over the protein position inside the crowder solution can potentially be a very expensive part of the postprocessing approach. The first approximation of FMAP is to use points on a cubic grid for the averaging over  $\mathbf{R}$ , assuming that the crowder configuration is generated from a simulation with periodic boundary conditions. We further separated the grid points where the protein would



Taylor expansion. The energy of a charge  $q$  at position  $\mathbf{r}$  is  $qf(\mathbf{r})$ . Suppose that this charge is distributed, with amounts  $\{\rho_i\}$  at a set of grid points  $\{\mathbf{n}_i\}$ . The energy of the distributed charges is  $\sum_i \rho_i f(\mathbf{n}_i)$ . The Taylor expansion of the latter in terms of the displacements  $\delta_i \equiv \mathbf{n}_i - \mathbf{r}$  is

$$\sum_i \rho_i f(\mathbf{r} + \delta_i) = f(\mathbf{r}) \sum_i \rho_i + \frac{\partial f(\mathbf{r})}{\partial \mathbf{r}} \cdot \sum_i \rho_i \delta_i + \sum_i \rho_i \delta_i \cdot \frac{\partial^2 f(\mathbf{r})}{\partial \mathbf{r} \partial \mathbf{r}} \cdot \delta_i + \dots \quad (11)$$

For this result to be exact up to the second order in  $\delta_i$ , we must have

$$\sum_i \rho_i = q; \sum_i \rho_i \delta_i = 0; \sum_i \rho_i \delta_i \delta_i = 0 \quad (12)$$

which constitute 10 independent linear equations for  $\{\rho_i\}$ . A unique solution for  $\{\rho_i\}$  can be found if  $q$  is distributed to 10 grid points. We chose the 10 grid points in the following way (Figure 3): (i) start with the eight grid points forming the

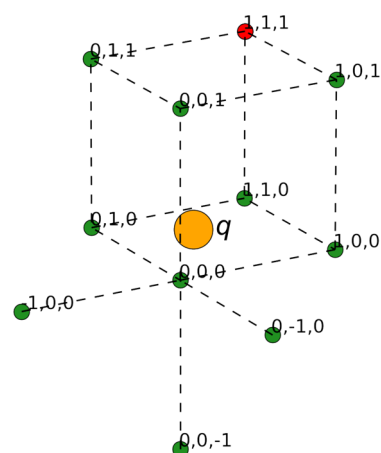


**Figure 3.** Selection of 10 grid points for distributing an atomic charge  $q$ . The eight grid points forming the smallest enclosing cube are labeled with index 0 or 1 in each direction. In the case shown, the grid point at (0, 0, 0) is closest to  $q$ , whereas the grid point (shown red) at (1, 1, 1) is farthest from  $q$ . All but the last grid point, plus the three external nearest neighbors of (0, 0, 0), at (−1, 0, 0), (0, −1, 0), and (0, 0, −1), are included for charge distribution.

smallest enclosing cube, and remove the one farthest from  $q$ ; (ii) identify the one closest to  $q$ , and then add the three nearest neighbors outside the enclosing cube.

To save time for the charge distribution, we precomputed the distribution for a full charge (i.e.,  $q = 1$ ) located at each position on a subgrid. The subgrid consisted of 1000 positions, generated with 1/10th of the original grid spacing  $\Delta$ , to sample the enclosing cube. For each atomic charge  $q_j$ , we located the nearest point on the subgrid and then took its precomputed charge distribution  $\{\rho_i\}$ . The latter, when multiplied by  $q_j$ , and the associated grid points  $\{\mathbf{n}_i\}$  then allowed for the distribution of the atomic charge.

We computed the potential function  $f(\mathbf{n})$  by exhaustively enumerating the contributions of each crowder atom to the grid points within the cutoff distance. A main intended use of FMAP is for studying different test proteins in selected crowder solutions.<sup>31</sup> For this purpose we can compute  $f(\mathbf{n})$  and its Fourier transform  $F(\mathbf{k})$  once and save for later use on different

test proteins. This computation is affordable at  $\Delta = 0.6$  Å. Here for the optimization of FMAP, we needed results at smaller  $\Delta$ . Instead of trying to speed up the computation of  $f(\mathbf{n})$ , we found an alternative solution, based on the fact that the energy can be calculated by either multiplying the crowders' potential with the protein's charges, as presented above, or vice versa. We confirmed that the two ways of calculating the energy gave essentially identical results, at least at  $\Delta \leq 0.6$  Å. While there are multiple crowder molecules within the grid, there is only a single protein molecule. Therefore, computing the potential of the protein is much faster than that of the crowders. The results presented below for  $\Delta < 0.6$  Å (other than those on timing) were all obtained by treating the test protein as the source of potential.

**2.4. Implementation of FMAP.** In FMAP, we evaluate the correlation function of eq 8 via FFT, taking advantage of the fact that, in Fourier space, the correlation function is a direct product:

$$C(\mathbf{k}) = F(\mathbf{k}) G^*(\mathbf{k}) \quad (13)$$

After the forward Fourier transforms of  $f(\mathbf{n})$  and  $g(\mathbf{n})$  and then the inverse Fourier transform of  $C(\mathbf{k})$ , we obtain the values of  $c(\mathbf{m})$  at all the grid points, allowing the Boltzmann average over  $\mathbf{R}$  to be calculated at once. We used the free library FFTW (version 3.3; double precision)<sup>40</sup> for computing the discrete Fourier transforms.

As explained already, the protein–crowder interaction energy used here involves four correlation functions: one for the hard-core repulsion, two for the soft attraction, and one for the electrostatic interaction. The values of these terms at the grid points were all saved on disk for repeated later use, such as different combinations of terms or scaling of individual terms.

**2.5. Test Proteins and Their Conformations.** We studied two proteins, cytochrome  $b_{562}$  and chymotrypsin inhibitor 2 (CI2), in the native and unfolded states, and two pairs of proteins, barnase:barstar and the  $\epsilon$  and  $\theta$  subunits of the *Escherichia coli* DNA polymerase III holoenzyme (Figure 4A–D), in the unbound and bound states. In all there were 10 distinct test protein systems. Eight of these were studied previously under crowding by spherical or ellipsoidal particles.<sup>6,31,41</sup> For each system, we took one conformation (i.e., the first of an ensemble collected from molecular dynamics simulations) for the study here. In future applications of FMAP, averaging over orientation and conformation of the test protein as well as over the crowder configuration will need to be carried out in order to obtain convergent results.

The two new systems added here are native and unfolded CI2. Their conformations were generated from room-temperature and high-temperature simulations (293 and 550 K), respectively, following the protocol of a previous study.<sup>42</sup> Briefly, the initial structure was from Protein Data Bank (PDB) entry 2CI2 (residues 20–83),<sup>43</sup> with mutations L20M, I49A, and I56A introduced to match the sequence in an experimental study of crowding effects on folding stability.<sup>14</sup> The protein was solvated by TIP3P water molecules and  $\text{Na}^+$  and  $\text{Cl}^-$  ions at 0.05 M (plus counterions that neutralized the charge of CI2) in a box with a side length of 66 (or 110) Å for the 293 (or 550) K simulation. The simulation at either 293 or 550 K was run using the GROMACS (version 4.5.4) program,<sup>44</sup> with the Amber99SB force field<sup>45</sup> and a time step of 2 or 1 fs, and at constant pressure or volume. All bond lengths involving hydrogen atoms were constrained. Long-range electrostatic interactions were treated by the particle mesh Ewald method<sup>38</sup>



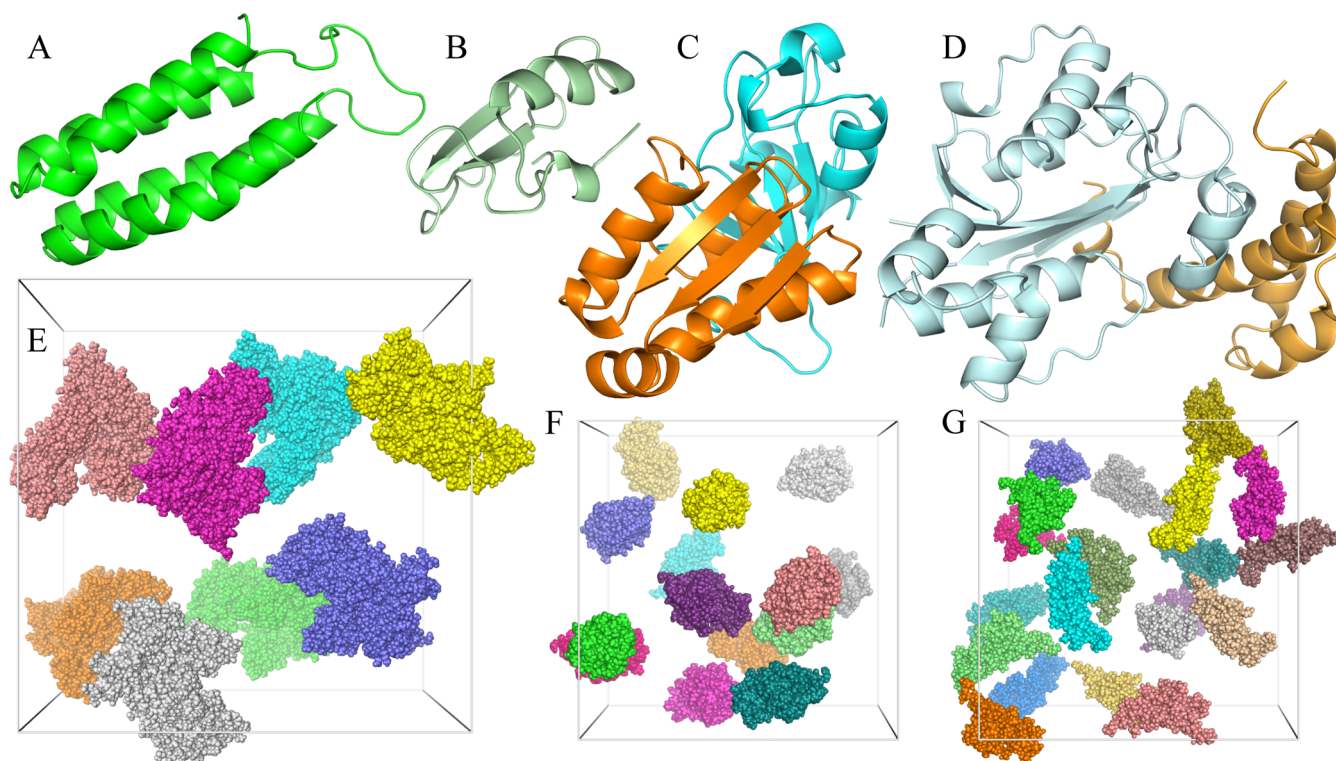


**Figure 4.** Test proteins and crowders studied here. (A) Cytochrome  $b_{562}$ . (B) CI2. (C) The barnase:barstar complex. (D) The  $\epsilon:\theta$  complex. (E) Eight copies of BSA in a  $(200 \text{ \AA})^3$  box. (F) Fourteen copies of lysozyme in a  $(150 \text{ \AA})^3$  box. (G) Twenty copies of dextran 10K in a  $(150 \text{ \AA})^3$  box.

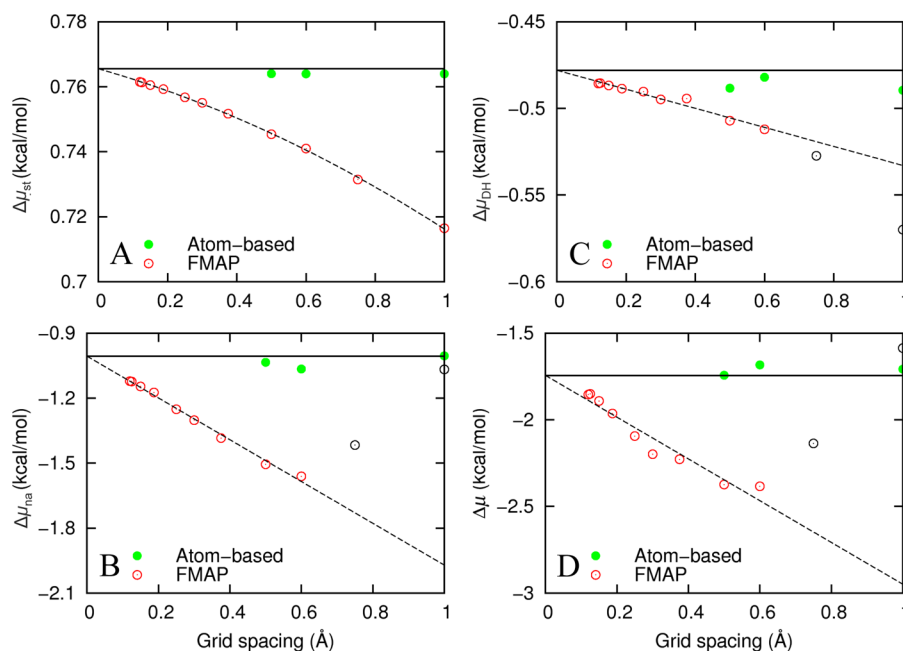


**Figure 5.** Grid-spacing dependences of FMAP and atom-based results for native cytochrome  $b_{562}$  in 100 g/L of lysozyme (with a configuration generated by random placement). (A)  $\Delta\mu_{st}$ . (B)  $\Delta\mu_{na}$ . (C)  $\Delta\mu_{DH}$ . (D)  $\Delta\mu$ . Open and closed circles display FMAP and atom-based results, respectively. Dashed lines (curve) are linear (quadratic) fits using data displayed as red circles. Note that the extrapolated FMAP results at 0 grid spacing, represented by solid horizontal lines, agree closely with those from the atom-based method. All the FMAP results here and in Figure 6 were obtained by treating the test protein as the source of potential when evaluating the soft interactions.

with a grid spacing of  $1.6 \text{ \AA}$  and a direct-space cutoff of  $10 \text{ \AA}$ . A cutoff of  $10 \text{ \AA}$  was used for evaluation of Lennard-Jones interactions. The snapshot at 100 (or 10) ns in the 293 (or 550) K simulation was used for the conformation of native (unfolded) CI2.

**2.6. Generation of Crowder Configurations.** We studied three kinds of crowders: bovine serum albumin (BSA), lysozyme, and dextran 10K (Figure 4E–G). The structure of BSA was modeled by homology using MODELER,<sup>46</sup> with residues 25–607 of the sequence (UniProtKB P02769) aligned

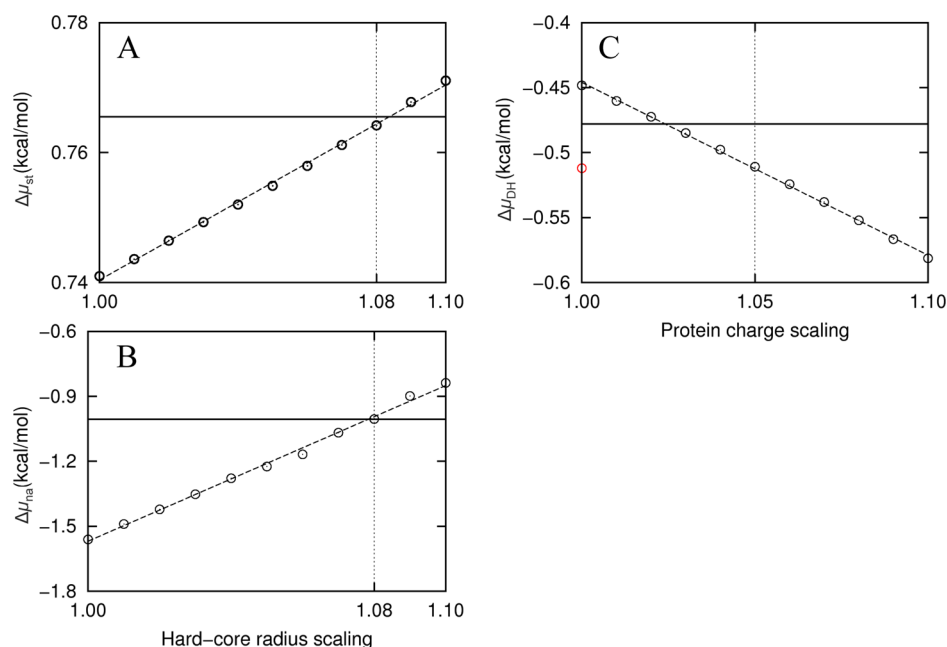


**Figure 6.** Corrections of FMAP at 0.6 Å grid spacing, illustrated using the results for native cytochrome  $b_{562}$  in 100 g/L of lysozyme. (A) Correcting for  $\Delta\mu_{st}$  by inflating the hard-core radii when detecting for protein–crowder clash. The extrapolated benchmark is shown as a solid horizontal line; the FMAP results calculated at 0.6 Å grid spacing but with hard-core radii inflated by 1% to 10% are shown as circles. (B)  $\Delta\mu_{na}$  calculated after filtering of grid points using inflated radii. (C)  $\Delta\mu_{DH}$  at  $I = 0.15$  M. The value before filtering of grid points is shown as a red circle. After filtering with 8% radius inflation,  $\Delta\mu_{DH}$  had a smaller magnitude than the extrapolated benchmark. Scaling up by  $\sim 3\%$  would correct the underestimate in this case, but on average 5% correction is needed at  $I = 0.15$  M for all the protein–crowder combinations studied.

to the structure of the human protein in PDB entry 1AO6.<sup>47</sup> The structure of lysozyme was taken from PDB entry 1AKI.<sup>48</sup> Dextran (molecular weight 9923.8) was built with 61 monosaccharide units<sup>49</sup> using Amber parameters (<http://www.pharmacy.manchester.ac.uk/bryce/amber>). BSA at 110 g/L, lysozyme at 100 g/L, and dextran at 100 g/L were created by placing eight copies in a box with a side length of 200 Å, 14 copies in a box with a side length of 150 Å, and 20 copies in a box with a side length of 150 Å. In each case, two crowder configurations were studied. One was obtained by randomly placing the crowder molecules into the box while ensuring no clash between the molecules.<sup>31</sup> The other was taken from a subsequent molecular dynamics simulation similar to that described above for C12 at 293 K. The snapshots used for BSA, lysozyme, and dextran were at 70, 95, and 10 ns, respectively, of the simulations. In addition, we generated a crowder configuration for dextran at 200 g/L by randomly placing 40 copies in the (150 Å)<sup>3</sup> box.

### 3. RESULTS

We carried out FMAP calculations for the combinations of the 10 test protein systems and seven distinct crowder configurations at grid spacings ranging from 1.0 to 0.12 Å. For the  $\epsilon:\theta$  complex interacting with dextran at 200 g/L, a very low fraction of clash-free placements rendered the results spurious. The FMAP results for the remaining 69 protein–crowder combinations are all reliable. For a subset of these combinations, we also applied the atom-based method to verify that the 0.6 Å grid spacing is adequate for the Boltzmann average over  $\mathbf{R}$  and also to provide a benchmark for assessing the accuracy of FMAP.

Accuracy was assessed on the Boltzmann average of the total interaction energy, which yields the excess chemical potential  $\Delta\mu$ , as well as on the Boltzmann averages calculated with

individual terms of the interaction energy selectively included, all at  $T = 298$  K. We loosely refer to the quantities yielded by the latter Boltzmann averages as components of  $\Delta\mu$ . Specifically, the steric component,  $\Delta\mu_{st}$ , is defined through

$$\exp(-\Delta\mu_{st}/k_B T) = \langle \exp(-U_{st}/k_B T) \rangle_0 \quad (14)$$

whereas the nonpolar-attraction and electrostatic components are defined through

$$\exp(-\Delta\mu_{na}/k_B T) = \langle \exp(-U_{na}/k_B T) \rangle_1 \quad (15)$$

$$\exp(-\Delta\mu_{DH}/k_B T) = \langle \exp(-U_{DH}/k_B T) \rangle_1 \quad (16)$$

Note that the sum of these three components does not equal  $\Delta\mu$ , because  $U_{na}$  and  $U_{DH}$  are not uncorrelated. Indeed, grid points where  $U_{DH}$  is most negative (and thus make the most electrostatic contribution to  $\Delta\mu$ ) are often also where  $U_{na}$  has large negative values. As a result,  $\Delta\mu$  tends to be more negative than expected from additivity.

**3.1. Benchmark Results Obtained from Extrapolation to 0 Grid Spacing.** Figure 5 displays the dependences of  $\Delta\mu$  and its components on the grid spacing  $\Delta$  for native cytochrome  $b_{562}$  in 100 g/L of lysozyme. The  $\Delta$  dependences for this and other protein–crowder systems are all apparently linear when  $\Delta \leq 0.6$  Å. For  $\Delta\mu_{st}$  in particular, the calculated values were so precise that a curvature was discernible in the dependence on  $\Delta$ . We thus fitted  $\Delta\mu_{na}$ ,  $\Delta\mu_{DH}$ , and  $\Delta\mu$  to a linear function of  $\Delta$  (including only data at  $\Delta \leq 0.6$  Å) and  $\Delta\mu_{st}$  to a quadratic function of  $\Delta$  (including all data).

Given the good quality of these fits, we expect that the extrapolated values at  $\Delta = 0$  should be free of discretization errors. Indeed, the extrapolated values agree closely with those calculated by the atom-based method (with  $\Delta = 0.5$  or 0.6 Å). The agreement of the atom-based results themselves at these two grid spacings verifies that  $\Delta = 0.6$  Å is sufficient for the

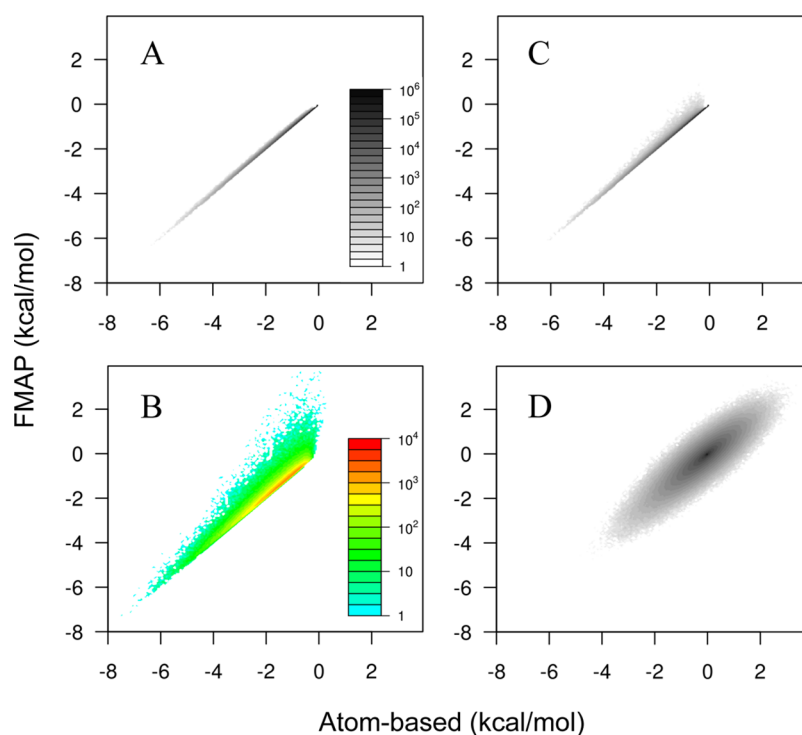


**Figure 7.** Accuracy assessment of FMAP values for  $U_{na}$  and  $U_{DH}$  at the individual grid points against the atom-based method, illustrated on native cytochrome  $b_{562}$  in 100 g/L of lysozyme (with the latter treated as the source of potential when evaluating the soft interactions;  $\Delta = 0.6$  Å and  $I = 0.15$  M). The results are shown as two-dimensional histograms, where the abscissa represents bins of atom-based interaction energies at 0.06 kcal/mol intervals, and the ordinate represents the FMAP counterparts, and the gray or color scale represents the number of (true or nominal) clash-free grid points in a two-dimensional cell. True clash-free grid points are those identified as such by the atom-based method. Nominal clash-free grid points are those identified by FMAP, without or with the 8% radius inflation. This inflation serves to filter a subset of the former nominal clash-free grid points. (A) At the true clash-free grid points, the FMAP values for  $U_{na}$  were highly accurate, as shown by significant densities only in the diagonal cells. (B) Among the grid points filtered through the radius inflation, FMAP values for  $U_{na}$  were skewed toward the less negative direction; there was also a subset with strongly negative  $U_{na}$  values, which led to an overestimated magnitude for  $\Delta\mu_{na}$ . (C) After filtering, the histogram for the remaining nominal clash-free grid points looks very similar to that calculated at the true clash-free grid points. (D) Densities in off-diagonal cells indicate inaccuracy in the corrected FMAP results for  $U_{DH}$ , but the nearly symmetric distribution of the densities with respect to the diagonal would lead to significant error cancellation in calculating  $\Delta\mu_{DH}$ .

discretization of  $\mathbf{R}$  (this method became prohibitively expensive at lower grid spacings). Hereafter, we will use the extrapolated FMAP results as benchmarks for assessing the accuracy of FMAP at finite grid spacing.

**3.2. Corrections of FMAP Results at 0.6 Å Grid Spacing.** For all 69 protein–crowder combinations studied, we found a negative slope in the dependence of  $\Delta\mu_{st}$  on  $\Delta$ . This observation suggests that FMAP systematically underestimated the fraction of clashed grid points, perhaps due to rounding off of hard-core regions when the protein and crowders were mapped to the grid. A way to compensate such round off is to inflate the hard-core radii. Figure 6A shows that radius inflation does have the desired effect for native cytochrome  $b_{562}$  in 100 g/L of lysozyme. An 8% inflation brings the FMAP result for  $\Delta\mu_{st}$  at  $\Delta = 0.6$  Å into agreement with the extrapolated benchmark. The amount of radius inflation needed showed very little variation among the different protein–crowder combinations.

With  $\Delta = 0.6$  Å, FMAP systematically overestimated the magnitude of  $\Delta\mu_{na}$  (Figure 5B). The grid points that are filtered by the radius inflation are positions where the protein would have close contact with one or more crowder molecules. It is likely that, at a subset of these grid points,  $U_{na}$  has large negative values (see below). Filtering these grid points would thus be expected to reduce the magnitude of  $\Delta\mu_{na}$ . Figure 6B

shows that, indeed, the magnitude of  $\Delta\mu_{na}$  decreases as the radius scaling factor is increased. Note that  $U_{na}$  at all the grid points was calculated once and then used for obtaining all the  $\Delta\mu_{na}$  results when the amount of radius inflation was varied. To our pleasant surprise, agreement with the extrapolated benchmark for  $\Delta\mu_{na}$  is reached also at 8% radius inflation. Again, the radius scaling factor is stable among the different protein–crowder combinations. We thus settled on an 8% radius inflation for the corrections of both the hard-core and soft interactions.

After the filtering with the 8% radius inflation,  $\Delta\mu_{DH}$  calculated over the remaining clash-free grid points at  $\Delta = 0.6$  Å had an underestimated magnitude (Figure 6C). As a correction, we scaled up the magnitude of  $\Delta\mu_{DH}$  (Figure 6C), which is equivalent to a scaling of the protein atomic charges. The charge scaling factor (denoted  $\xi$ ) is also pretty constant among the different protein–crowder combinations, averaging at 1.05 for 0.15 M ionic strength (denoted  $I$ ). The charge scaling factor has a distinct dependence on ionic strength, approaching 1 as  $I$  increases. This trend is to be expected, since  $U_{DH}$  decays faster at higher  $I$  so the correction needed should reduce accordingly. The average charge scaling factor over the ionic strength range of 0.05 to 0.25 M can be represented by the relation  $\xi = 1 + 0.025I^{-0.4}$ .

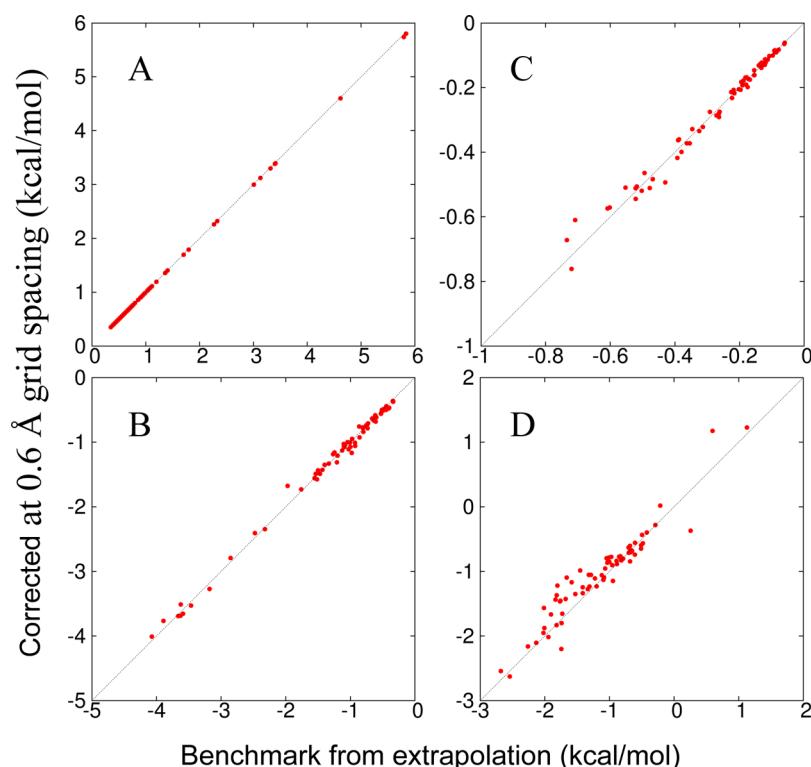


**Figure 8.** Comparison of corrected FMAP results at  $\Delta = 0.6$  Å for the 69 protein–crowder combinations against the extrapolated benchmarks. (A)  $\Delta\mu_{st}$ . (B)  $\Delta\mu_{na}$ . (C)  $\Delta\mu_{DH}$  at  $I = 0.15$  M. (D)  $\Delta\mu$ . Results were obtained by treating the test protein as the source of potential when evaluating the soft interactions. The numerical values and identities of the protein–crowder systems are listed in Table 1.

To verify that the corrections for the components of the excess chemical potential went to the root of the discretization errors, we investigated how the corrections impacted the values of the corresponding interactions at the individual grid points. Again we use native cytochrome  $b_{562}$  in 100 g/L of lysozyme for illustration. According to the atom-based method, of the  $15.63 \times 10^6$  grid points generated with  $\Delta = 0.6$  Å,  $4.29 \times 10^6$  grid points, or 27.5%, are clash-free. Without radius inflation, FMAP yielded a 28.5% clash-free fraction, which covered all the true clash-free grid points, but also included  $0.17 \times 10^6$  false-positive grid points. With the 8% radius inflation, FMAP filtered 81% of the false positives along with just 0.8% of the true clash-free grid points.

As shown in Figure 7A, at the true clash-free grid points, the FMAP values for  $U_{na}$  were highly accurate when benchmarked against the atom-based method. At the grid points that were filtered by the 8% radius inflation, the would-be FMAP values for  $U_{na}$  overall tended to be not as negative as would be determined by the atom-based method if clash were disregarded (Figure 7B). However, as we suspected, among these to-be filtered grid points, there was a small subset with strongly negative  $U_{na}$  values. It is indeed this subset of grid points that was responsible for the overestimation in the magnitude of  $\Delta\mu_{na}$  when FMAP was uncorrected. After filtering with the 8% radius inflation, the range and distribution of the FMAP values for  $U_{na}$  (Figure 7C) are very similar to those determined by the atom-based method. On the other hand, after the filtering of grid points and the scaling of magnitudes (5% at  $I = 0.15$  M), the FMAP values for  $U_{DH}$  still have a 0.29 kcal/mol root-mean-square-deviation (RMSD) from the atom-based counterparts. Importantly, the deviations are roughly even in the opposite directions (Figure 7D), so that  $\Delta\mu_{DH}$

resulting from their Boltzmann average has a much small error (0.03 kcal/mol).

After the corrections with the 8% radius inflation and the 5% magnitude inflation for  $U_{DH}$ , the FMAP results at  $\Delta = 0.6$  Å for the components of  $\Delta\mu$  and for  $\Delta\mu$  itself become highly accurate for all the 69 protein–crowder combinations studied when compared to the extrapolated benchmarks (Figure 8 and Table 1). Specifically, with the test protein treated as the source of potential when evaluating the soft interactions, the RMSDs for  $\Delta\mu_{st}$ ,  $\Delta\mu_{na}$ ,  $\Delta\mu_{DH}$ , and  $\Delta\mu$  are 0.009, 0.07, 0.02, and 0.23 kcal/mol, respectively. The last value is even somewhat lower than the RMSD, 0.30 kcal/mol, of the uncorrected FMAP results at  $\Delta = 0.15$  Å and would require  $\Delta = 0.12$  Å without corrections. With the corrections listed above, essentially identical results were obtained when the crowders were treated as the source of potential.

**3.3. Gain in Speed at 0.6 Å Grid Spacing.** In Figure 9, we display the computational times when FMAP was run on an AMD Opteron 6174 processor with either the crowders or the test protein treated as the source of potential (labeled as Crowders:Protein and Protein:Crowders, respectively), as well as the times for the FFT portion alone, at grid spacings from 1.0 to 0.15 Å, for native cytochrome  $b_{562}$  in 100 g/L of lysozyme. At  $\Delta = 0.6$  Å, the FFT portion took 7.5 s, but the “overhead,” mostly the calculation of  $f(\mathbf{n})$  and (to a lesser extent)  $g(\mathbf{n})$ , took even longer for the Protein:Crowders implementation (total time at 18.6 s) but especially for the Crowders:Protein implementation (total time at 121 s). As a comparison, using the atom-based method, the calculation of  $U_{DH}$  alone took 417 000 s. As noted above, in future applications we will calculate  $f(\mathbf{n})$  and save its Fourier

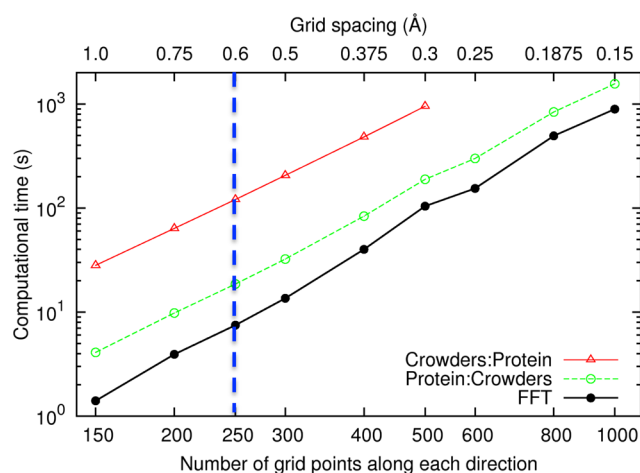


Table 1. Extrapolated Benchmarks and Corrected FMAP Results at  $\Delta = 0.6$  Å (in kcal/mol) for the 69 Protein–Crowder Combinations

protein	crowder	$\Delta\mu_{st}$		$\Delta\mu_{na}$		$\Delta\mu_{DH}$		$\Delta\mu$	
		extrap.	$\Delta$ at 0.6	extrap.	$\Delta$ at 0.6	extrap.	$\Delta$ at 0.6	extrap.	$\Delta$ at 0.6
b562n	BSA	0.596	0.595	−0.615	−0.583	−0.179	−0.191	−0.831	−0.764
	BSAsim	0.471	0.470	−0.447	−0.500	−0.122	−0.130	−1.806	−1.220
	Dex100	1.198	1.193	−1.334	−1.331	−0.226	−0.214	−1.002	−0.853
	Dex100sim	0.737	0.734	−0.998	−1.071	−0.136	−0.128	−0.957	−0.903
	Dex200	3.410	3.395	−3.664	−3.691	−0.602	−0.571	−1.452	−0.986
	Lys	0.765	0.764	−1.006	−1.006	−0.478	−0.511	−1.744	−2.201
b562u	Lyssim	0.542	0.541	−0.620	−0.665	−0.430	−0.493	−1.945	−2.016
	BSA	0.723	0.722	−0.608	−0.682	−0.090	−0.090	−0.288	−0.282
	BSAsim	0.562	0.562	−0.480	−0.486	−0.060	−0.061	−0.421	−0.398
	Dex100	1.361	1.356	−1.432	−1.429	−0.188	−0.178	−0.682	−0.604
	Dex100sim	0.900	0.898	−1.267	−1.187	−0.132	−0.123	−0.971	−0.776
	Dex200	5.793	5.739	−3.893	−3.767	−0.709	−0.610	1.128	1.226
CI2n	Lys	0.976	0.975	−1.101	−1.028	−0.363	−0.372	−1.528	−1.350
	Lyssim	0.675	0.675	−0.978	−1.166	−0.202	−0.205	−1.818	−1.832
	BSA	0.414	0.413	−0.399	−0.467	−0.097	−0.101	−0.606	−0.741
	BSAsim	0.350	0.350	−0.337	−0.375	−0.079	−0.083	−0.511	−0.648
	Dex100	0.767	0.764	−1.086	−1.047	−0.139	−0.131	−0.850	−0.773
	Dex100sim	0.521	0.520	−0.744	−0.754	−0.091	−0.085	−0.672	−0.703
CI2u	Dex200	2.329	2.321	−2.854	−2.793	−0.390	−0.363	−1.816	−1.369
	Lys	0.522	0.522	−0.863	−0.757	−0.191	−0.193	−1.286	−1.055
	Lyssim	0.383	0.382	−0.500	−0.495	−0.125	−0.128	−1.119	−1.058
	BSA	0.540	0.540	−0.408	−0.479	−0.119	−0.122	0.255	−0.371
	BSAsim	0.438	0.438	−0.342	−0.363	−0.085	−0.088	−0.510	−0.596
	Dex100	0.980	0.978	−1.027	−1.111	−0.140	−0.132	−0.604	−0.558
bn	Dex100sim	0.661	0.659	−0.726	−0.709	−0.092	−0.086	−0.496	−0.435
	Dex200	3.129	3.121	−3.179	−3.272	−0.494	−0.464	−1.335	−1.274
	Lys	0.695	0.694	−0.806	−0.783	−0.172	−0.174	−1.045	−0.797
	Lyssim	0.503	0.502	−0.513	−0.502	−0.112	−0.113	−0.700	−0.713
	BSA	0.568	0.567	−0.633	−0.668	−0.197	−0.207	−1.765	−1.464
	BSAsim	0.455	0.454	−0.493	−0.512	−0.132	−0.139	−1.308	−1.233
bn:bs	Dex100	1.115	1.111	−1.554	−1.558	−0.195	−0.183	−1.083	−1.096
	Dex100sim	0.722	0.719	−1.399	−1.350	−0.131	−0.123	−1.093	−1.130
	Dex200	3.400	3.385	−3.625	−3.512	−0.518	−0.506	−1.662	−1.095
	Lys	0.722	0.721	−1.101	−1.068	−0.216	−0.218	−1.741	−1.800
	Lyssim	0.504	0.503	−0.663	−0.634	−0.131	−0.132	−1.010	−0.786
	BSA	0.859	0.857	−1.245	−1.159	−0.271	−0.286	−1.835	−1.436
bs	BSAsim	0.607	0.607	−0.805	−0.769	−0.168	−0.176	−1.198	−1.232
	Dex100	1.797	1.790	−2.477	−2.407	−0.346	−0.328	−1.757	−1.454
	Dex100sim	1.060	1.059	−1.971	−1.676	−0.182	−0.169	−1.904	−1.666
	Dex200	5.836	5.801	−4.074	−4.009	−0.734	−0.672	0.595	1.175
	Lys	1.086	1.085	−1.536	−1.491	−0.503	−0.519	−2.681	−2.543
	Lyssim	0.747	0.746	−0.857	−0.925	−0.313	−0.322	−1.412	−1.337
$\epsilon$	BSA	0.486	0.485	−0.523	−0.550	−0.086	−0.091	−0.681	−0.662
	BSAsim	0.397	0.397	−0.443	−0.443	−0.061	−0.065	−0.651	−0.683
	Dex100	0.914	0.911	−1.208	−1.312	−0.178	−0.168	−1.066	−0.955
	Dex100sim	0.612	0.611	−0.974	−0.949	−0.121	−0.112	−1.029	−0.810
	Dex200	3.008	2.998	−3.465	−3.529	−0.553	−0.510	−1.414	−1.246
	Lys	0.638	0.637	−1.043	−1.000	−0.521	−0.544	−2.262	−2.161
$\epsilon:\theta$	Lyssim	0.451	0.451	−0.626	−0.615	−0.393	−0.418	−2.021	−1.952
	BSA	0.800	0.799	−0.798	−0.841	−0.264	−0.281	−0.946	−1.148
	BSAsim	0.582	0.581	−0.525	−0.560	−0.155	−0.162	−2.013	−1.567
	Dex100	1.704	1.696	−1.761	−1.730	−0.291	−0.275	−0.890	−0.838
	Dex100sim	1.029	1.026	−1.500	−1.436	−0.180	−0.169	−1.224	−1.109
	Dex200	4.617	4.601	−3.590	−3.655	−0.522	−0.511	−0.213	0.019
	Lys	1.047	1.045	−1.198	−1.208	−0.469	−0.483	−1.730	−1.655
	Lyssim	0.704	0.703	−0.925	−1.058	−0.325	−0.334	−2.007	−1.876
	BSA	1.091	1.089	−0.929	−1.008	−0.379	−0.399	−1.320	−1.054
	BSAsim	0.727	0.727	−0.598	−0.616	−0.223	−0.232	−2.543	−2.627

Table 1. continued

protein	crowder	$\Delta\mu_{st}$		$\Delta\mu_{na}$		$\Delta\mu_{DH}$		$\Delta\mu$	
		extrap.	$\Delta$ at 0.6	extrap.	$\Delta$ at 0.6	extrap.	$\Delta$ at 0.6	extrap.	$\Delta$ at 0.6
$\theta$	Dex100	2.268	2.261	−2.321	−2.346	−0.387	−0.360	−0.681	−0.845
	Dex100sim	1.364	1.360	−1.515	−1.575	−0.218	−0.207	−0.835	−0.788
	Lys	1.404	1.403	−1.470	−1.491	−0.720	−0.761	−2.134	−2.105
	Lyssim	0.945	0.943	−1.126	−1.128	−0.354	−0.373	−1.678	−1.427
	BSA	0.538	0.536	−0.451	−0.468	−0.263	−0.291	−0.884	−0.887
	BSAsim	0.445	0.445	−0.337	−0.364	−0.175	−0.198	−0.788	−0.802
	Dex100	0.987	0.984	−1.091	−1.075	−0.155	−0.146	−0.705	−0.629
	Dex100sim	0.679	0.677	−0.733	−0.785	−0.108	−0.102	−0.482	−0.565
	Dex200	3.318	3.299	−3.629	−3.686	−0.608	−0.574	−1.032	−0.866
	Lys	0.684	0.683	−0.752	−0.737	−0.262	−0.275	−1.584	−1.168
	Lyssim	0.480	0.480	−0.488	−0.506	−0.154	−0.161	−0.815	−0.830



**Figure 9.** Computational times of FMAP on native cytochrome  $b_{562}$  in 100 g/L of lysozyme at  $\Delta$  from 1.0 to 0.15 Å. Traces labeled “Crowders:Protein” and “Protein:Crowders” represent total times with the crowders and the test protein, respectively, treated as the source of potential; the trace labeled “FFT” represents the times for the FFT portion of the FMAP calculations.

transform for selected crowder systems so that this overhead would not constitute a new cost.

Focusing on the FFT portion, the computational time at  $\Delta = 0.15$  Å was 893.1 s, a 120-fold increase over that at  $\Delta = 0.6$  Å. Therefore, with the corrections presented above for  $\Delta = 0.6$  Å, we not only achieve higher accuracy but also gain more than 100-fold in speed when compared to the use of a 0.15 Å fine grid spacing. Attaining the same accuracy through using an even finer grid spacing of 0.12 Å would increase the computational time 220-fold.

#### 4. DISCUSSION

We have presented an accurate and efficient implementation of the FMAP (EFT-based Modeling of Atomistic Proteins-crowder interactions) method, based on corrections of results at a relatively coarse grid spacing. Because we represent the crowder molecules on a grid, the core of FMAP (involving FFT operations) would not suffer any loss of computational speed when crowded conditions of cellular compartments are more and more realistically modeled, e.g., through increasing the number of crowder species and other types of complexity. We are thus hopeful that FMAP will become a practical tool for realistic modeling of protein folding and binding in cell-like environments.

A number of important applications of FMAP can be anticipated. The first is the parametrization of the protein–crowder interaction energy.<sup>25</sup> With the speed of FMAP, we can afford to do extensive parametrization, e.g., against experimental results for protein folding stability.<sup>14–19</sup> Similarly, we will be able to include much more extensive conformational sampling of the test protein in the absence of crowders for predicting the effects of crowding on folding and binding. As noted previously,<sup>30,50</sup> the postprocessing approach underlying FMAP is premised on thorough crowder-free sampling for ensuring sufficient overlap with the conformational space of the protein under crowding.

FMAP is in essence a particle-insertion method<sup>51</sup> and as such is effective only if there is a statistically significant clash-free fraction. This condition can be broken when inserting a large protein (or complex) into a very concentrated crowder solution, as was found here for the  $\epsilon:\theta$  complex interacting with dextran at 200 g/L. One way out, as demonstrated in our previously study,<sup>31</sup> is to carry out FMAP calculations at lower crowder concentrations and then extrapolate the results to the desired high crowder concentration.

Discretization in general and FFT in particular are widely used in treating intramolecular and intermolecular interactions, such as charge–charge interaction. The optimization of accuracy and speed by correcting for results at a relatively coarse grid spacing perhaps can be instructive for improving other methods that employ discretization of space. In this regard we note an improvement orthogonal to ours, for the smooth particle mesh Ewald method, that involved doing calculations over two coarse grids that were staggered at half grid spacing and then averaging the results.<sup>52</sup>

#### AUTHOR INFORMATION

##### Corresponding Author

\*Phone: (850) 645-1336. Fax: (850) 644-7244. E-mail: hzhou4@fsu.edu.

##### Notes

The authors declare no competing financial interest.

#### ACKNOWLEDGMENTS

This work was supported by National Institutes of Health Grant GM88187. We thank Dr. Bernard Brooks for calling our attention to ref 52.

## ■ REFERENCES

- (1) Zhou, H. X.; Rivas, G.; Minton, A. P. Macromolecular crowding and confinement: biochemical, biophysical, and potential physiological consequences. *Annu. Rev. Biophys.* **2008**, *37*, 375–397.
- (2) Feig, M.; Sugita, Y. Reaching new levels of realism in modeling biological macromolecules in cellular environments. *J. Mol. Graphics Modell.* **2013**, *45*, 144–156.
- (3) Zhou, H. X. Influence of crowded cellular environments on protein folding, binding, and oligomerization: biological consequences and potentials of atomistic modeling. *FEBS Lett.* **2013**, *587*, 1053–1061.
- (4) Cheung, M. S.; Klimov, D.; Thirumalai, D. Molecular crowding enhances native state stability and refolding rates of globular proteins. *Proc. Natl. Acad. Sci. U.S.A.* **2005**, *102*, 4753–4758.
- (5) Minh, D. D.; Chang, C. E.; Trylska, J.; Tozzini, V.; McCammon, J. A. The influence of macromolecular crowding on HIV-1 protease internal dynamics. *J. Am. Chem. Soc.* **2006**, *128*, 6006–6007.
- (6) Qin, S.; Zhou, H. X. Atomistic modeling of macromolecular crowding predicts modest increases in protein folding and binding stability. *Biophys. J.* **2009**, *97*, 12–19.
- (7) Qin, S.; Minh, D. D. L.; McCammon, J. A.; Zhou, H.-X. Method to predict crowding effects by postprocessing molecular dynamics trajectories: application to the flap dynamics of HIV-1 protease. *J. Phys. Chem. Lett.* **2010**, *1*, 107–110.
- (8) Qin, S.; Zhou, H.-X. Generalized fundamental measure theory for atomistic modeling of macromolecular crowding. *Phys. Rev. E* **2010**, *81*, 031919.
- (9) Dong, H.; Qin, S.; Zhou, H. X. Effects of macromolecular crowding on protein conformational changes. *PLoS Comput. Biol.* **2010**, *6*, e1000833.
- (10) Mittal, J.; Best, R. B. Dependence of protein folding stability and dynamics on the density and composition of macromolecular crowders. *Biophys. J.* **2010**, *98*, 315–320.
- (11) Dhar, A.; Samiotakis, A.; Ebbinghaus, S.; Nienhaus, L.; Homouz, D.; Gruebele, M.; Cheung, M. S. Structure, function, and folding of phosphoglycerate kinase are strongly perturbed by macromolecular crowding. *Proc. Natl. Acad. Sci. U.S.A.* **2010**, *107*, 17586–17591.
- (12) Kang, M.; Roberts, C.; Cheng, Y. H.; Chang, C. E. A. Gating and intermolecular interactions in ligand-protein association: coarse-grained modeling of HIV-1 protease. *J. Chem. Theory Comput.* **2011**, *7*, 3438–3446.
- (13) Nagarajan, S.; Amir, D.; Grupi, A.; Goldenberg, D.; Minton, A.; Haas, E. Modulation of functionally significant conformational equilibria in adenylate kinase by high concentrations of trimethylamine oxide attributed to volume exclusion. *Biophys. J.* **2011**, *100*, 2991–2999.
- (14) Miklos, A. C.; Sarkar, M.; Wang, Y.; Pielak, G. J. Protein crowding tunes protein stability. *J. Am. Chem. Soc.* **2011**, *133*, 7116–7120.
- (15) Benton, L. A.; Smith, A. E.; Young, G. B.; Pielak, G. J. Unexpected effects of macromolecular crowding on protein stability. *Biochemistry* **2012**, *51*, 9773–9775.
- (16) Wang, Y.; Sarkar, M.; Smith, A. E.; Krois, A. S.; Pielak, G. J. Macromolecular crowding and protein stability. *J. Am. Chem. Soc.* **2012**, *134*, 16614–16618.
- (17) Miklos, A. C.; Sumpter, M.; Zhou, H. X. Competitive interactions of ligands and macromolecular crowders with maltose binding protein. *PLoS One* **2013**, *8*, e74969.
- (18) Sarkar, M.; Smith, A. E.; Pielak, G. J. Impact of reconstituted cytosol on protein stability. *Proc. Natl. Acad. Sci. U.S.A.* **2013**, *110*, 19342–19347.
- (19) Guzman, I.; Gelman, H.; Tai, J.; Gruebele, M. The extracellular protein VlsE is destabilized inside cells. *J. Mol. Biol.* **2014**, *426*, 11–20.
- (20) Zhou, H. X. SAXS/SANS probe of intermolecular interactions in concentrated protein solutions. *Biophys. J.* **2014**, *106*, 771–773.
- (21) Goldenberg, D. P.; Argyle, B. Self crowding of globular proteins studied by small-angle x-ray scattering. *Biophys. J.* **2014**, *106*, 895–904.
- (22) Goldenberg, D. P.; Argyle, B. Minimal effects of macromolecular crowding on an intrinsically disordered protein: a small-angle neutron scattering study. *Biophys. J.* **2014**, *106*, 905–914.
- (23) Douglas, J. F.; Dudowicz, J.; Freed, K. F. Crowding induced self-assembly and enthalpy-entropy compensation. *Phys. Rev. Lett.* **2009**, *103*, 135701.
- (24) Jiao, M.; Li, H. T.; Chen, J.; Minton, A. P.; Liang, Y. Attractive protein-polymer interactions markedly alter the effect of macromolecular crowding on protein association equilibria. *Biophys. J.* **2010**, *99*, 914–923.
- (25) McGuffee, S. R.; Elcock, A. H. Diffusion, crowding & protein stability in a dynamic molecular model of the bacterial cytoplasm. *PLoS Comput. Biol.* **2010**, *6*, e1000694.
- (26) Rosen, J.; Kim, Y. C.; Mittal, J. Modest protein-crowder attractive interactions can counteract enhancement of protein association by intermolecular excluded volume interactions. *J. Phys. Chem. B* **2011**, *115*, 2683–2689.
- (27) Feig, M.; Sugita, Y. Variable interactions between protein crowders and biomolecular solutes are important in understanding cellular crowding. *J. Phys. Chem. B* **2012**, *116*, 599–605.
- (28) Zhou, H. X. Polymer crowders and protein crowders act similarly on protein folding stability. *FEBS Lett.* **2013**, *587*, 394–397.
- (29) Zhou, H. X.; Qin, S. Simulation and modeling of crowding effects on the thermodynamic and kinetic properties of proteins with atomic details. *Biophys. Rev.* **2013**, *5*, 207–215.
- (30) Qin, S.; Mittal, J.; Zhou, H. X. Folding free energy surfaces of three small proteins under crowding: validation of the postprocessing method by direct simulation. *Phys. Biol.* **2013**, *10*, 045001.
- (31) Qin, S.; Zhou, H. X. FFT-based method for modeling protein folding and binding under crowding: benchmarking on ellipsoidal and all-atom crowders. *J. Chem. Theory Comput.* **2013**, *9*, 4633–4643.
- (32) Ravichandran, S.; Madura, J. D.; Talbot, J. A Brownian dynamics study of the initial stages of hen egg-white lysozyme adsorption at a solid interface. *J. Phys. Chem. B* **2001**, *105*, 3610–3613.
- (33) Kim, Y. C.; Hummer, G. Coarse-grained models for simulations of multiprotein complexes: application to ubiquitin binding. *J. Mol. Biol.* **2008**, *375*, 1416–1433.
- (34) Morris, G. M.; Huey, R.; Lindstrom, W.; Sanner, M. F.; Belew, R. K.; Goodsell, D. S.; Olson, A. J. AutoDock4 and AutoDockTools4: automated docking with selective receptor flexibility. *J. Comput. Chem.* **2009**, *30*, 2785–2791.
- (35) Ando, T.; Skolnick, J. Crowding and hydrodynamic interactions likely dominate *in vivo* macromolecular motion. *Proc. Natl. Acad. Sci. U.S.A.* **2010**, *107*, 18457–18462.
- (36) Cornell, W. D.; Cieplak, P.; Bayly, C. I.; Gould, I. R.; Merz, K. M.; Ferguson, D. M.; Spellmeyer, D. C.; Fox, T.; Caldwell, J. W.; Kollman, P. A. A second generation force field for the simulation of proteins, nucleic acids, and organic molecules. *J. Am. Chem. Soc.* **1995**, *117*, 5179–5197.
- (37) Mattson, W.; Rice, B. M. Near-neighbor calculations using a modified cell-linked list method. *Comput. Phys. Commun.* **1999**, *119*, 135–148.
- (38) Essmann, U.; Perera, L.; Berkowitz, M. L.; Darden, T.; Lee, H.; Pedersen, L. G. A smooth particle mesh Ewald method. *J. Chem. Phys.* **1995**, *103*, 8577–8593.
- (39) Baker, N. A.; Sept, D.; Joseph, S.; Holst, M. J.; McCammon, J. A. Electrostatics of nanosystems: application to microtubules and the ribosome. *Proc. Natl. Acad. Sci. U.S.A.* **2001**, *98*, 10037–10041.
- (40) Frigo, M.; Johnson, S. G. The design and implementation of FFTW3. *Proc. IEEE* **2005**, *93*, 216–231.
- (41) Batra, J.; Xu, K.; Qin, S.; Zhou, H. X. Effect of macromolecular crowding on protein binding stability: modest stabilization and significant biological consequences. *Biophys. J.* **2009**, *97*, 906–911.
- (42) Tjong, H.; Zhou, H. X. The folding transition-state ensemble of a four-helix bundle protein: helix propensity as a determinant and macromolecular crowding as a probe. *Biophys. J.* **2010**, *98*, 2273–2280.
- (43) McPhalen, C. A.; James, M. N. Crystal and molecular structure of the serine proteinase inhibitor CI-2 from barley seeds. *Biochemistry* **1987**, *26*, 261–269.

- (44) Hess, B.; Kutzner, C.; van der Spoel, D.; Lindahl, E. GROMACS 4: algorithms for highly efficient, load-balanced, and scalable molecular simulation. *J. Chem. Theory Comput.* **2008**, *4*, 435–447.
- (45) Hornak, V.; Abel, R.; Okur, A.; Strockbine, B.; Roitberg, A.; Simmerling, C. Comparison of multiple Amber force fields and development of improved protein backbone parameters. *Proteins* **2006**, *65*, 712–725.
- (46) Eswar, N.; Webb, B.; Marti-Renom, M. A.; Madhusudhan, M. S.; Eramian, D.; Shen, M.-Y.; Pieper, U.; Sali, A., Comparative protein structure modeling using MODELLER. *Curr. Protoc. Protein Sci.* **2007**, Chapter 2, Unit 2.9.
- (47) Sugio, S.; Kashima, A.; Mochizuki, S.; Noda, M.; Kobayashi, K. Crystal structure of human serum albumin at 2.5 Å resolution. *Protein Eng.* **1999**, *12*, 439–446.
- (48) Artymiuk, P. J.; Blake, C. C. F.; Rice, D. W.; Wilson, K. S. The structures of the monoclinic and orthorhombic forms of hen egg-white lysozyme at 6 Å resolution. *Acta Crystallogr., Sect. B* **1982**, *38*, 778–783.
- (49) Pathiaseril, A.; Woods, R. J. Relative energies of binding for antibody-carbohydrate-antigen complexes computed from free-energy simulations. *J. Am. Chem. Soc.* **2000**, *122*, 331–338.
- (50) Qin, S.; Zhou, H. X. Effects of macromolecular crowding on the conformational ensembles of disordered proteins. *J. Phys. Chem. Lett.* **2013**, *4*, 3429–3434.
- (51) Widom, B. Some topics in theory of fluids. *J. Chem. Phys.* **1963**, *39*, 2808–2812.
- (52) Cerutti, D. S.; Duke, R. E.; Darden, T. A.; Lybrand, T. P. Staggered mesh ewald: an extension of the smooth particle-mesh Ewald method adding great versatility. *J. Chem. Theory Comput.* **2009**, *5*, 2322–2338.